

# Short Injector Quantum Cascade Lasers

Kale J. Franz, *Student Member, IEEE*, Peter Q. Liu, James J. J. Raftery, Matthew D. Escarra, *Student Member, IEEE*, Anthony J. Hoffman, *Student Member, IEEE*, Scott Sheridan Howard, *Member, IEEE*, Yu Yao, Yamac Dikmelik, Xiaojun Wang, Jen-Yu Fan, Jacob B. Khurgin, and Claire Gmachl, *Senior Member, IEEE*

**Abstract**—We report our study on the effects of shortened quantum cascade (QC) laser injector regions. While conventional short-wavelength QC lasers typically have around seven or more injector region quantum wells, we investigate QC structures with three and two injector wells. Improvements in threshold currents, output powers, and wall-plug efficiencies are expected for fundamental reasons. At heat sink temperatures near 80 K, we observe threshold current densities less than  $0.5 \text{ kA/cm}^2$ , nearly 4 W peak output power, and wall-plug efficiencies in excess of 20%. At room temperature, we see threshold current densities around  $2.3 \text{ kA/cm}^2$ , output powers in excess of 1 W, and wall-plug efficiencies around 7.6%. We also observe new effects in midinfrared QC lasers, such as a pronounced negative differential resistance, pulse instabilities, and multiple and varied turn-off mechanisms. These effects result from the greatly abbreviated injector regions with highly discrete states.

**Index Terms**—Midinfrared, negative differential resistance, quantum cascade (QC) laser, short injector.

## I. INTRODUCTION

**P**ROGRESS in quantum cascade (QC) laser development has cemented the role of these semiconductor emitters for applications at midinfrared wavelengths. The latest performance advances have primarily been demonstrated through improved understanding and implementation of thermal management strategies; QC stacks in a buried heterostructure waveguide mounted epitaxial-side down on diamond submounts have surpassed watt-level power in continuous wave mode at room temperature [1], [2]. While impressive, these lasers are based on fundamental QC design strategies that date to 2001. Since

that time, no significant improvement has been realized by implementing a fundamentally different QC design.

The 2001 design advance [3] that led to the first CW room temperature QC laser [4] is the so-called “double-phonon” structure. Here, a structural modification is made to the QC active region. The double-phonon active region is composed of at least three wells, where each of the three lowest coupled active region quantum ground states are spaced one longitudinal optical (LO) phonon energy apart; this allows enhanced relaxation out of the lower laser state [4]. The extra energy drop imparted by the secondary LO phonon transition also mitigates thermal backfilling of the lower laser level [5].

While much attention has been paid to improving QC performance by modifications to the *active region* structure, we here focus on a reexamination of the role of *injector regions* in QC laser performance. Since injector regions themselves are not the source of photon generation, prior work in the field has examined the possibility of eliminating injector regions altogether. In these “injectorless” QC structures, active regions are successively stitched together without the aid of injector region energy states. The first such device was the work of Wanke *et al.*, where a chirped superlattice design emitting at  $11 \mu\text{m}$  lased up to 195 K [6]. More recently, Friedrich, Katz, *et al.* have removed the injector wells from the more conventional single- and double-phonon active region structures [7], [8]. These injectorless QC lasers have shown low threshold current densities and pulsed lasing at room temperature over a range of midinfrared wavelengths. And while not purely injectorless, it is worth noting that today’s best performing THz QC lasers [9], [10] have significantly shorter injector regions (one or two wells) than the first THz QC lasers [11].

In conventional QC structures, the injector regions do, however, serve a multitude of important functions. Indeed, the absence of these features may well have limited the performance of previous injectorless designs. Among the key functions of QC injector regions are:

- efficient injection of electrons into the upper laser state;
- isolation of the upper laser state from the continuum;
- Bragg reflection of the upper laser state, preventing electron escape by tunneling;
- facilitation of electrons in “relaxing” out of the active region;
- spatial and energetic separation of the lower laser state from the downstream electron pool;
- providing space over which electrons can gain energy relative to the conduction band edge; and
- providing a convenient space for doping to reduce impurity scattering.

Manuscript received May 11, 2009; revised July 23, 2009. Current version published February 26, 2010. This work was supported in part by DARPA EMIL and by the Mid-Infrared Technologies for Health and the Environment (MIRTHE) Center (NSF-ERC # EEC-0540832). The work of K. J. Franz was supported by the NSF Graduate Research Fellowship Program and by the Princeton University Wallace Fellowship.

K. J. Franz, P. Q. Liu, J. J. J. Raftery, M. D. Escarra, A. J. Hoffman, Y. Yao, and C. Gmachl are with the Department of Electrical Engineering, Princeton University, Princeton, NJ 08544 USA (e-mail: kfranz@princeton.edu; qiangliu@princeton.edu; jjraftery@gmail.com; escarra@princeton.edu; ajhoffma@princeton.edu; yuyao@princeton.edu; cgmachl@princeton.edu).

S. S. Howard is with the Department of Electrical Engineering, Princeton University, Princeton, NJ 08544 USA, and also with the School of Engineering and Applied Physics, Cornell University, Ithaca, NY 14853 USA (e-mail: showard@princeton.edu).

Y. Dikmelik and J. B. Khurgin are with the Department of Electrical Engineering, Johns Hopkins University, Baltimore, MD 21218 USA (e-mail: yamac@jhu.edu; jakek@jhu.edu).

X. Wang and J.-Y. Fan are with AdTech Optics, Inc., City of Industry, CA 91748 USA (e-mail: xiaojun.wang@atoptics.com; jenyu.fan@atoptics.com).

Color versions of one or more of the figures in this paper are available online at <http://ieeexplore.ieee.org>.

Digital Object Identifier 10.1109/JQE.2009.2030896

Given the many important functions of QC injector regions, we examine QC structures with highly minimalized injector regions. Conventional midinfrared QC laser designs typically have between five and nine injector wells (shorter wavelength designs generally employ more injector wells). Here, we study short-wavelength ( $\lambda_0 \sim 5 \mu\text{m}$ ) QC designs that have either two or three injector wells.

## II. THEORETICAL FRAMEWORK

The motivation for minimizing injector region length is compelling. Key among the performance parameters of high quality lasers are small threshold current densities, large slope efficiencies, and large wall-plug efficiencies. In examining the relations for each of these performance parameters, we see that injector length plays a key role. For example, the low temperature threshold current density

$$J_{\text{th}} = \delta\mathcal{E}_{ul} \frac{\epsilon_0 \lambda_0 n_{\text{eff}}}{4\pi q} \frac{\alpha_m + \alpha_w}{(\eta_{\text{inj}} \tau_{\text{eff}} - (1 - \eta_{\text{inj}}) \tau_\ell)} \frac{L_{ac}}{z_{ul}^2 \Gamma N_p} \quad (1)$$

where  $\delta\mathcal{E}_{ul}$  is the full-width-at-half-maximum (FWHM) of the gain spectrum,  $\epsilon_0$  is the permittivity of free space,  $\lambda_0$  is the free space wavelength,  $n_{\text{eff}}$  is the effective refractive index of the optical mode,  $q$  is the electron charge,  $\alpha_m + \alpha_w$  is the combined mirror and waveguide loss,  $z_{ul}$  is the optical dipole matrix element between the upper and lower laser states,  $L_{ac}$  is the thickness of the QC active core,  $\Gamma$  is the optical confinement factor for the lasing mode, and  $N_p$  is the number of QC periods in the active core. The effective upper state lifetime  $\tau_{\text{eff}} = \tau_u(1 - \tau_\ell/\tau_{ul})$ , where  $\tau_u$  is the upper laser state composite lifetime,  $\tau_\ell$  is the lower laser state composite lifetime, and  $\tau_{ul}$  is the transition lifetime between the upper and lower laser states. The electron injection efficiency into the upper laser state  $\eta_{\text{inj}}$  is included, and the term  $(1 - \eta_{\text{inj}})$  implies that all electrons not injected into the upper laser state pass through the lower laser state.

We can see from (1) for  $J_{\text{th}}$  that, for any fixed value of  $L_{ac}/\Gamma$  (i.e. fixed active core thickness and waveguide configuration), lower thresholds are achieved when more QC periods  $N_p$  are squeezed into the QC stack. Ideally then, one should shorten the overall QC period length. But the length of the QC active region is somewhat fixed for any given emission wavelength and active region design strategy. The only practical place to decrease the QC period length is the injector region. However, when considering short injector QC structures, one must be mindful that shortening the injector regions can potentially lead to the deleterious effect of decreased upper laser state injection efficiency. This may occur, for example, via more readily populating the active region state immediately above the upper laser state, out of which electrons can easily scatter (nonradiatively) to energy states below the upper laser state.

As injector lengths are shortened and more QC periods are added to the active core, we can likewise expect an increase in total output power  $P$ , given as [12]

$$P = N_p \frac{\mathcal{E}_{\text{ph}}}{q} \eta_{\text{inj}} \eta_m \frac{\tau_{\text{eff}}}{\tau_{\text{eff}} + \tau_\ell} \frac{\alpha_m}{\alpha_m + \alpha_w} (J - J_{\text{th}}) A \quad (2)$$

where  $\mathcal{E}_{\text{ph}}$  is the photon energy,  $J$  is the injection current density, and  $A$  is the laser device area.<sup>1</sup> The term  $\tau_{\text{eff}}/(\tau_{\text{eff}} + \tau_\ell)$  represents the differential efficiency of the laser transition [13], which effectively accounts for reabsorption of photons due to the lower laser level having a finite electron population. The “modal efficiency”  $\eta_m$  is defined as [14]

$$\eta_m = \frac{\left(\sum_i^{N_p} \Gamma_i\right)^2}{N_p \sum_i^{N_p} \Gamma_i^2} \quad (3)$$

which weights the reduction of photon generation caused by (vertical) spatial hole burning.<sup>1</sup> The individual, per-period confinement factor  $\Gamma_i$  is effectively the “local field coefficient”  $f^2(z)$ , where  $f(z)$  is the electric field profile of the optical mode in the growth direction  $z$  normalized such that  $\max(f(z)) = 1$ . Two direct effects of shortened injector regions on  $P$  become clear. We have already demonstrated that shortened injectors reduce  $J_{\text{th}}$ , which is accompanied by a commensurate increase in  $P$  for any  $J > J_{\text{th}}$ . We also see a linear increase in  $P$  as we fit more QC periods  $N_p$  into the same mode profile (i.e., as  $\eta_m$  remains constant).

The wall-plug efficiency  $\eta_{\text{wp}}$  is yet another performance metric that should be improved by shortened injectors. The wall-plug efficiency can be expressed as a product of constituent terms as

$$\eta_{\text{wp}} = \frac{\mathcal{E}_{\text{ph}}}{\mathcal{E}_{\text{ph}} + \Delta_{\text{inj}} + \frac{IR_{\text{series}}}{N_p}} \frac{\tau_{\text{eff}}}{\tau_{\text{eff}} + \tau_\ell} \times \frac{\alpha_m}{\alpha_m + \alpha_w} \frac{(J - J_{\text{th}})}{J} \eta_{\text{inj}} \eta_m \quad (4)$$

where  $\Delta_{\text{inj}}$  is the energy drop between the lower laser level in one active region and the upper laser level in the next downstream active region, and  $IR_{\text{series}}$  is the voltage drop across the device not attributable to the active core.<sup>1</sup> Insofar as there is some series resistance  $R_{\text{series}}$  for the device (from top and bottom contacts, for example), increasing  $N_p$  will decrease the net parasitic effect on  $\eta_{\text{wp}}$ . As in output power, increasing  $N_p$  also increases “current efficiency” for  $J > J_{\text{th}}$ .

As a final point, a reduction in the individual QC period length  $L_p = L_{ac}/N_p$  could ultimately lead to the ability to produce more total output power. With maximum output power  $P_{\text{max}} \propto J_{\text{max}} - J_{\text{th}}$ , a large “dynamic range” in operating current is desirable. The maximum current density  $J_{\text{max}}$  a QC laser can carry before a turn-off condition is reached can be defined as [15], [16]

$$J_{\text{max}} = \frac{qn_{\text{trans}}}{\tau_{\text{trans}}} \quad (5)$$

where  $\tau_{\text{trans}}$  is the total time needed for an electron to traverse one QC period and  $n_{\text{trans}}$  is the sheet density of electrons that participate in transport across the period. The total number of electrons present in the system  $n_s$  should equal  $n_{\text{trans}} + n_{\text{stationary}}$ , with  $n_s$  being the doping sheet density and  $n_{\text{stationary}}$  being the sheet density of conduction band electrons that do no contribute to current transport. The transit time  $\tau_{\text{trans}}$  can be simplistically thought of as comprising the

<sup>1</sup>The derivation of (2)–(4) makes use of assumptions that restrict the validity of these equations to injection currents near threshold.

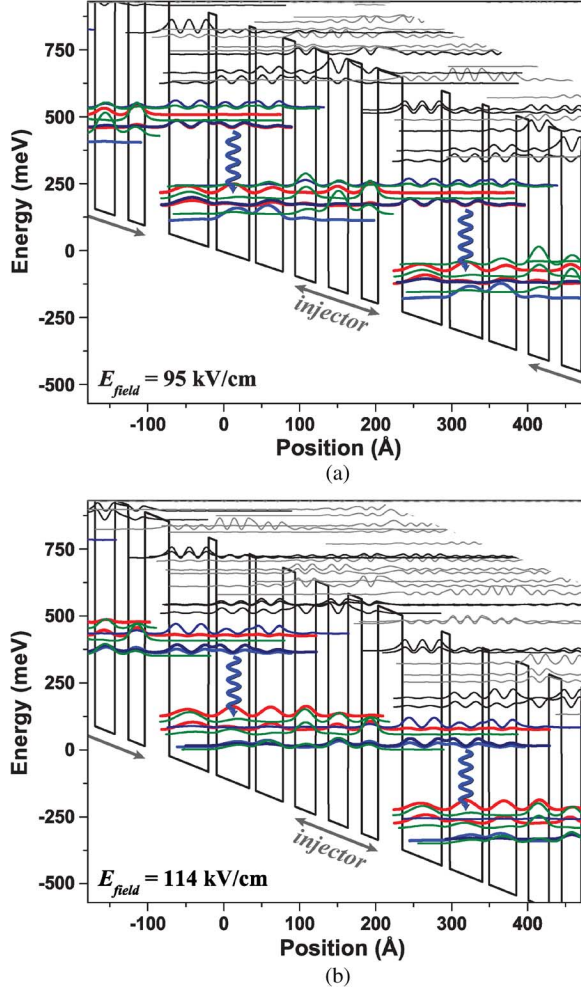


Fig. 1. QC structure with three injector wells and three active region wells. Electron transport leading to negative differential resistance is also observed starting at 95 kV/cm, (a). At 95 kV/cm the second energy level of one active region is in resonance with the downstream upper laser state at this field. The as-designed turn-on field is 114 kV/cm, (b).

active region transit time and the injector region transit time  $\tau_{inj}$ . One might intuitively reason that, with shorter injector regions,  $\tau_{inj}$  decreases, therefore increasing  $J_{max}$ . Expressed in another way,  $\tau_{trans}$  relates to the differential resistance over the active core (injectors and active regions)  $R_{ac}$  as

$$R_{ac} = \frac{V_{appl} \tau_{trans}}{qA n_{trans}} \quad (6)$$

where  $V_{appl}$  is the applied voltage. A shorter  $\tau_{trans}$  and, therefore, lower differential resistance means the upper laser state and injector ground state can remain in resonance over a larger range in current, increasing  $J_{max}$  and  $P_{max}$ .

When designing short injector QC lasers, one becomes particularly aware of the operating field  $E_{field}$ . In a QC structure,  $E_{field}$  is simply expressed as

$$E_{field} = \frac{\mathcal{E}_{ph} + \Delta_{inj}}{qL_p} \quad (7)$$

Thus, for a fixed emission wavelength and optimally designed  $\Delta_{inj}$ ,  $E_{field}$  and QC period length  $L_p$  are inversely proportional.

The consequential higher operating field for shortened injector regions often results in more difficulty in designing confinement for the upper laser state—which can be counteracted by use of high band-offset strained materials—and sometimes leads to laser reliability problems.

### III. QC LASER WITH THREE INJECTOR WELLS

#### A. Design and Fabrication

We designed a QC laser consisting of six quantum wells per QC period—shown in the Fig. 1 conduction band diagram—with emission energy  $\mathcal{E}_{ph} = 239$  meV ( $\lambda_0 = 5.19$   $\mu\text{m}$ ) and energy defect  $\Delta_{inj} = 116$  meV. With three active region wells and three injector wells, the total period length  $L_p = 307$  Å, in contrast to  $L_p > 500$  Å for the best conventional QC structures [1]. The combination of energies and period length result in a turn-on field  $E_{field} = 114$  kV/cm. The layer sequence is, in angstroms starting from the injection barrier, **32/52/10.5/43/8.5/36/16/27/16.5/26/18/21.5**, where  $\text{Al}_{0.710}\text{In}_{0.290}\text{As}$  layers are in bold type,  $\text{In}_{0.638}\text{Ga}_{0.362}\text{As}$  layers are in plain type, and layers Si-doped  $n = 1.0 \times 10^{17} \text{ cm}^{-3}$  are underlined; the structure has an active core sheet density  $n_s = 1.1 \times 10^{11} \text{ cm}^{-2}$  per period. At 125 kV/cm, where the upper and lower laser states are somewhat isolated, we calculate  $\tau_u = 1.4$  ps,  $\tau_l = 0.5$  ps,  $\tau_{ul} = 5.6$  ps, and  $z_{ul} = 20.6$  Å, for a Figure of Merit  $\text{FoM} = \tau_{eff} z_{ul}^2 = 544 \text{ ps } \text{\AA}^2$  and  $\text{FoM}^* = \tau_{eff} z_{ul}^2 \mathcal{E}_{ph} = 130 \text{ ps } \text{\AA}^2 \text{ eV}^2$ .

The laser was grown using metal-organic vapor phase epitaxy (MOVPE) on a low doped ( $n < 2 \times 10^{17} \text{ cm}^{-3}$ ) InP substrate. The QC active-injector sequence was repeated 50 times. The QC active core was surrounded on each side by  $0.12 \mu\text{m}$   $\text{In}_{0.53}\text{Ga}_{0.47}\text{As}$  Si-doped  $n = 0.5 \times 10^{17} \text{ cm}^{-3}$  to enhance gain region confinement factor. Following the  $\text{In}_{0.53}\text{Ga}_{0.47}\text{As}$  confinement layer, the top cladding consisted of  $2.5 \mu\text{m}$  InP Si-doped  $n = 0.5 \times 10^{17} \text{ cm}^{-3}$ ,  $0.7 \mu\text{m}$  InP Si-doped  $n = 80 \times 10^{17} \text{ cm}^{-3}$ ,  $0.1 \mu\text{m}$  InP Si-doped  $n = 200 \times 10^{17} \text{ cm}^{-3}$ , and finally  $0.06 \mu\text{m}$   $\text{In}_{0.53}\text{Ga}_{0.47}\text{As}$  Si-doped  $n = 500 \times 10^{17} \text{ cm}^{-3}$ . Standard quantum well gradings between bulk  $\text{In}_{0.53}\text{Ga}_{0.47}\text{As}$  and InP regions were used to assist electron transport across the bulk interfaces. For transitions from InP to  $\text{In}_{0.53}\text{Ga}_{0.47}\text{As}$ , the grading layer sequence (in angstroms) was **25/25/30/20/35/15/40/10/45/5**, where  $\text{Al}_{0.48}\text{In}_{0.52}\text{As}$  layers are in bold type and  $\text{In}_{0.53}\text{Ga}_{0.47}\text{As}$  layers are in plain type.

Ridge lasers with thin Au top contacts were fabricated using standard processes [17]; buried heterostructure (BH) devices with InP overgrowth were likewise fabricated. We also fabricated and tested electroluminescence (EL) mesas [17] designed to suppress optical feedback in order to study spontaneous emission properties of the structure.

#### B. Results and Discussion

We examined the light-current-voltage (LIV) properties of both EL mesas and ridge lasers. We observe a pronounced neg-

<sup>2</sup>The term  $\text{FoM}^*$  multiplies the traditional  $z^2 \tau_{eff}$  figure of merit by the laser photon energy, providing a basis of comparison for laser designs at different wavelengths, since the gain cross section is proportional to transition energy.

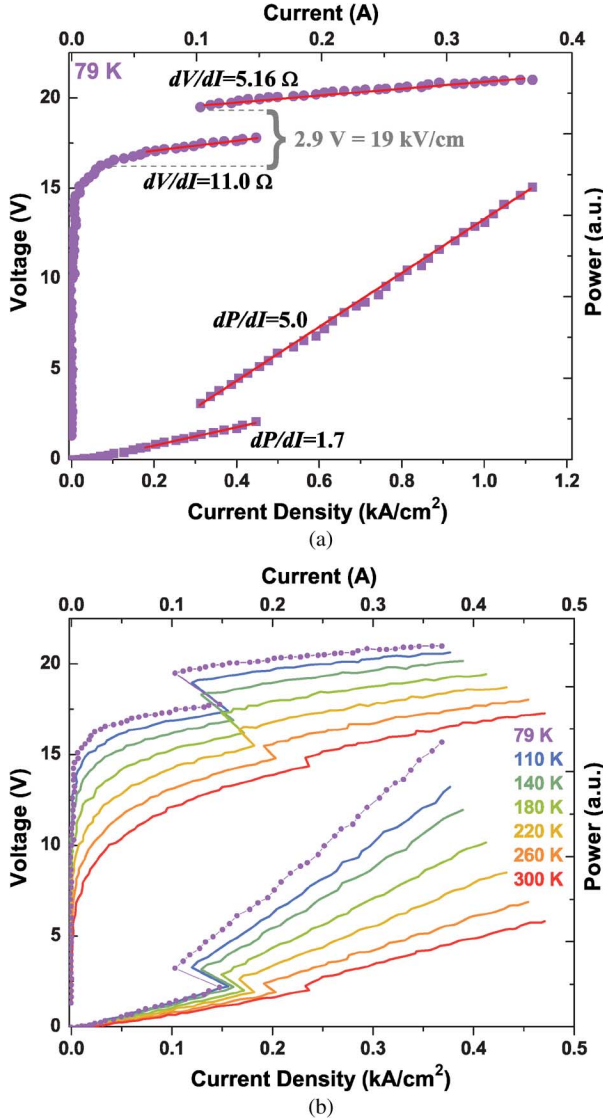


Fig. 2. Pulsed LIV data of electroluminescence mesas for the three injector well QC structure. The area of the tested device is  $0.033 \text{ mm}^2$ . Pronounced negative differential resistance is seen at low temperature (a) and persists through room temperature (b).

active differential resistance (NDR) feature in all devices. In EL mesas at a heat sink temperature  $T_{\text{sink}} = 80 \text{ K}$  and current densities near  $0.3 \text{ kA/cm}^2$ , we see a rapid  $1.7 \text{ V}$  ( $11 \text{ kV/cm}$ ) “jump,” as shown in Fig. 2(a). The voltage increase is accompanied by a reduction in current density of  $0.13 \text{ kA/cm}^2$ . After the NDR feature, the differential resistance  $dV/dI$  decreases by a factor of 2. We also observe in the light-current (LI) data that, after the NDR feature, the radiative efficiency  $dP/dI$  increases by a factor of 3. We furthermore see from Fig. 2(b) that the NDR persists through room temperature.

The NDR can be understood in that the two operating states—before the NDR feature and after—represent two different energy band configurations. At  $T_{\text{sink}} = 80 \text{ K}$ , the difference in turn-on of the two current paths is  $2.9 \text{ V}$  ( $19 \text{ kV/cm}$ ). Associating the current path in operation after the NDR feature with the band alignment at the design field of  $114 \text{ kV/cm}$ ,

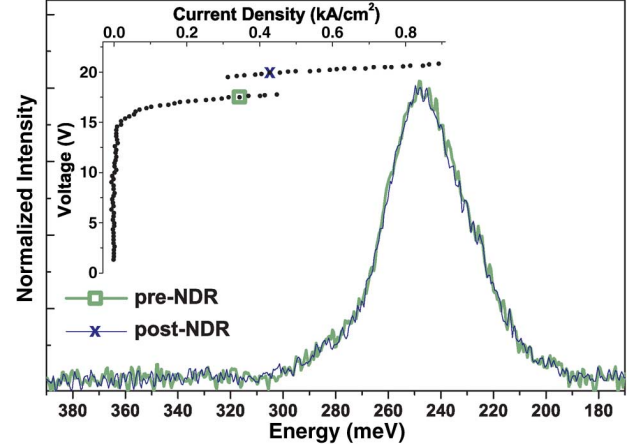


Fig. 3. Comparison of EL spectra at pre- and post-NDR operating points. The pre-NDR point, light-colored bold line, is at  $J = 0.34 \text{ kA/cm}^2$  and  $V = 17.5 \text{ V}$ . The post-NDR point, dark-colored narrow line, is at  $J = 0.43 \text{ kA/cm}^2$  and  $V = 19.9 \text{ V}$ . We observe no spectral distinction between the two operating points. The spectral resolution of the data is  $1 \text{ meV}$ .

the first current path operates with turn-on at  $95 \text{ kV/cm}$ . The energy diagram at  $95 \text{ kV/cm}$ , plotted in Fig. 1(a), elucidates a process of electron transport across the injector region after just a single phonon transition from the lower laser state. In this case,  $\Delta_{\text{inj}} = 49 \text{ meV}$ , rather than the  $116 \text{ meV}$  at  $114 \text{ kV/cm}$ .

Interestingly, this is strong evidence of current flow and light generation with the lowest state of one active region significantly below the upper laser state of the next downstream active region. At the lower field of  $95 \text{ kV/cm}$  in Fig. 1(a), most of the dopant electrons  $n_s$  are “trapped” in the lowest active region state (i.e.,  $n_{\text{stationary}} \approx n_s$ ). In contrast, at  $E_{\text{field}} = 114 \text{ kV/cm}$ ,  $n_{\text{trans}} \approx n_s$ . The NDR can thus be interpreted as the existence of two different values of  $J_{\text{max}}$ : one for the  $95 \text{ kV/cm}$  band alignment, and a second, larger  $J_{\text{max}}$  for the  $114 \text{ kV/cm}$  band alignment.

EL spectra collected at pre- and post-NDR points, as in Fig. 3, are absent any discernable spectral changes between the two operating points. We thus conclude that the upper and lower energy states of the optical transition remain the same between the two operating points. The field re-alignment changes only the configuration of the injector states relative to the active region states.

The data become all the more interesting for laser devices, i.e., with the inclusion of stimulated emission in the overall device behavior. Fig. 4(a) shows that no NDR is observed in the current-voltage (IV) data at  $80 \text{ K}$ . Rather, the NDR only appears at temperatures near and above  $140 \text{ K}$ . Fig. 4(b) shows the onset of NDR behavior with greater temperature resolution. Here, we see the NDR feature appear at  $130 \text{ K}$ , the first temperature where threshold current density is greater than the current density at which the NDR occurs ( $J_{\text{th}} > J_{\text{NDR}}$ ). Apparently, it is the presence of cavity photons (stimulated emission) that prevents the observation of NDR and locks the laser into the pre-NDR band configuration for  $T_{\text{sink}} < 130 \text{ K}$ . Also of note is that the laser exhibits two thresholds for  $T_{\text{sink}} = 130 \text{ K}$  and slightly above. The two thresholds directly result from the NDR—that is, the



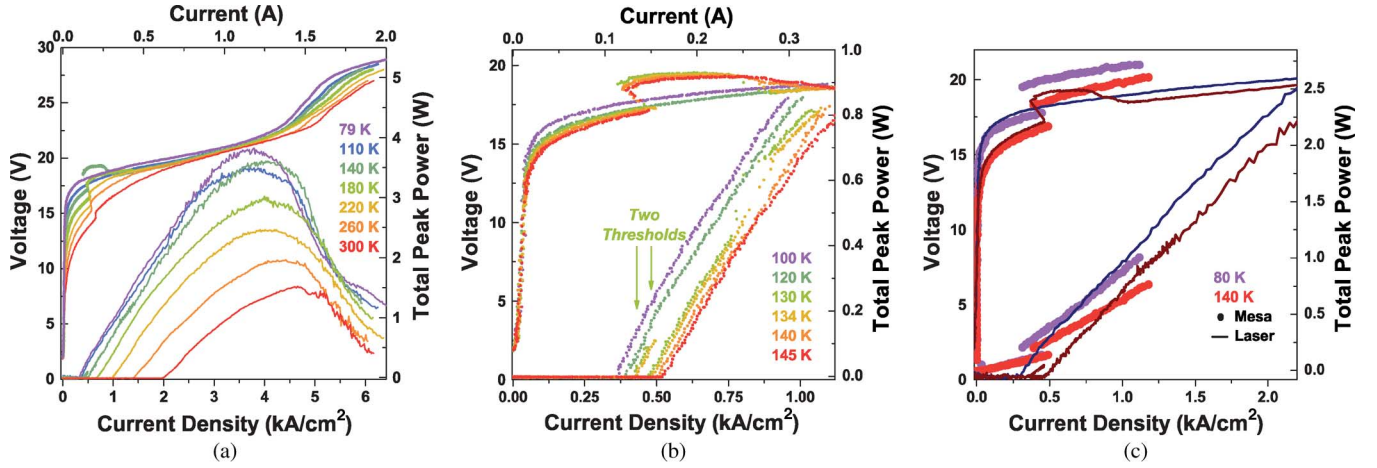


Fig. 4. LIV data for a representative three injector well  $10.4 \mu\text{m} \times 3 \text{ mm}$  ridge laser device. (a): NDR is observed, but only at elevated temperatures. (b): the NDR appears only for  $J_{\text{th}} > J_{\text{NDR}}$ , i.e. here for  $T_{\text{sink}} \geq 130 \text{ K}$ . Because of the NDR, we observe two thresholds for  $T_{\text{sink}} = 130 \text{ K}$  and slightly above. The comparison of LIV data from this laser device and EL data from Fig. 2(b), as in (c), shows the effect of cavity photon density on the current-voltage behavior.

decrease in pumping current as the energy level configuration realigns at the higher field.

Perhaps even more surprising, for  $T_{\text{sink}}$  corresponding to  $J_{\text{th}} > J_{\text{NDR}}$ , increasing cavity photon density actively “pulls down” the operating voltage. Effectively, the internal electric field decreases, returning the band configuration to the pre-NDR state. This, in fact, is a second form of NDR, where voltage decreases with increasing current, rather than the more typically thought-of NDR where current decreases with increasing voltage. The feature can plainly be seen in Fig. 4(c), where we compare LIV data from mesa and laser devices at  $T_{\text{sink}} = 80$  and  $140 \text{ K}$ .

The behavior of these two NDR features for laser devices can be explained by considering contributions to the total per period transport rate  $1/\tau_{\text{trans}}$ . We can simplify the total carrier transit time through a QC period  $\tau_{\text{trans}}$  as being the sum of active region and injector region transit times due to nonradiative processes such as phonon scattering—respectively,  $\tau_{\text{act}}$  and  $\tau_{\text{inj}}$ —and including a term  $\tau_{\text{stim}}$  that accounts for photon-assisted transport due to stimulated emission. The stimulated emission term effectively decreases the active region transit time

$$\tau_{\text{trans}} = (\tau_{\text{act}}^{-1} + \tau_{\text{stim}}^{-1})^{-1} + \tau_{\text{inj}}. \quad (8)$$

Here,  $\tau_{\text{act}}$  and  $\tau_{\text{stim}}$  are grouped in recognition that active region transport may be either by stimulated emission and/or non-radiative scattering. To explain the first NDR feature, where the temperature dependence of  $J_{\text{th}}$  affects the presence of this NDR, we return to our consideration of  $J_{\text{max}}$ . Stimulated emission significantly extends  $J_{\text{max}}$ , especially if the total nonradiative transport time is dominated by  $\tau_{\text{act}}$  (due to the long lifetime of the upper laser state) in the absence of stimulated emission. Thus, for temperatures below  $130 \text{ K}$  where no NDR is observed,  $J_{\text{max}}(E_{\text{field}} = 95 \text{ kV/cm})$  includes stimulated emission and is, therefore, large. For temperatures at and above  $130 \text{ K}$  where we see NDR,  $J_{\text{max}}(E_{\text{field}} = 95 \text{ kV/cm})$  is smaller since  $J_{\text{th}} < J_{\text{max}}$ .

To explain the second NDR feature, where voltage decreases with increasing current for  $T_{\text{sink}} \geq 130 \text{ K}$ , we again look to

the effect of stimulated emission on  $1/\tau_{\text{trans}}$  and  $J_{\text{max}}$ . Specifically, this behavior can be understood with the insight that  $J_{\text{max}}$  changes with the presence of stimulated emission. The dynamic shift of  $J_{\text{max}}$  results in the laser facing the option of two transport paths. For  $T_{\text{sink}} \geq 130 \text{ K}$ ,  $J_{\text{max}}$  at  $E_{\text{field}} = 114 \text{ kV/cm}$  is greater than  $J_{\text{th}}$ , but *once lasing has been established* due to the presence of stimulated emission,  $J_{\text{max}}$  at  $E_{\text{field}} = 95 \text{ kV/cm}$  is *also* greater than  $J_{\text{th}}$ . Now, with two available transport paths, the laser selects the path that leads to minimum operating power (and here, lower operating voltage). Thus, the presence of stimulated emission causes the laser to revert back to the lower field configuration.

After the second NDR feature, we observe a marked decrease in slope efficiency. In Fig. 5, we see that the slope efficiency for the low field band configuration [Fig. 1(a)] is nearly half that of the high field configuration [Fig. 1(b)]:  $2.8$  versus  $5.0 \text{ W/A}$ , respectively. This discrepancy is at least consistent with the factor of 3 observed in the EL case (Fig. 2). Although the exact origin is unclear, we can narrow the source of the difference down to either injection efficiency into the upper laser state or the laser transition efficiency, since  $(dP/dI) \propto \eta_{\text{inj}}(\tau_{\text{eff}}/(\tau_{\text{eff}} + \tau_{\ell}))$ , and no other terms in  $dP/dI$  change with a change in band structure configuration alone.

### C. Device Performance

Lasing occurs at  $\lambda_0 \approx 5.1 \mu\text{m}$  for  $T_{\text{sink}} = 79 \text{ K}$  and at  $\lambda_0 \approx 5.4 \mu\text{m}$  at room temperature, as shown in Fig. 6(a). For the ridge laser device described by the Fig. 4 data, pulsed total output power peaks at  $3.8 \text{ W}$  at  $80 \text{ K}$ , while room temperature output power is  $1.5 \text{ W}$ . Threshold current density is as low as  $313 \text{ A/cm}^2$  at  $80 \text{ K}$ , and reaches  $2.0 \text{ kA/cm}^2$  at room temperature. Fig. 6(b) explains this increase, with the rather low characteristic temperature  $T_0 = 113 \text{ K}$  for  $T_{\text{sink}}$  where  $J_{\text{th}} > J_{\text{NDR}}$ . However, for  $T_{\text{sink}}$  where  $J_{\text{th}} < J_{\text{NDR}}$ ,  $T_0$  is much higher at

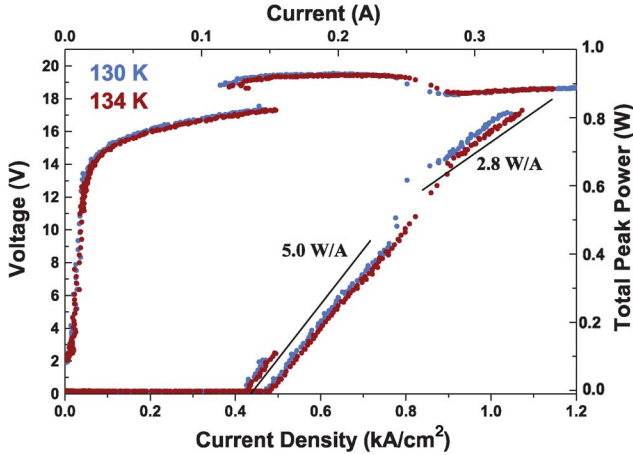


Fig. 5. LIV data near the transition  $J_{th} > J_{NDR}$ , here for  $T_{sink} = 130$  and  $134$  K. Different slope efficiencies are observed before and after the band configuration that results from the presence of stimulated emission. No significant change in slope efficiency is observed before and after the NDR point.

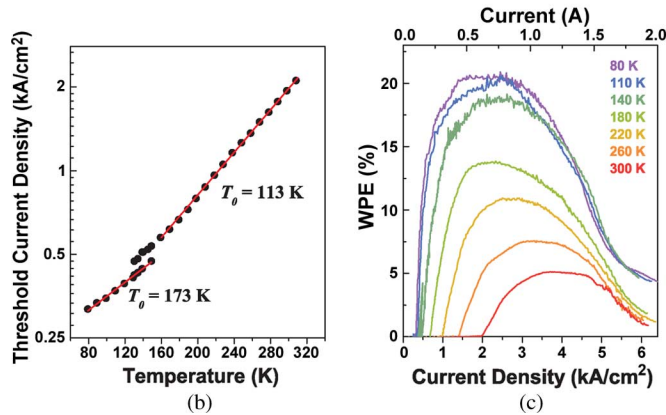
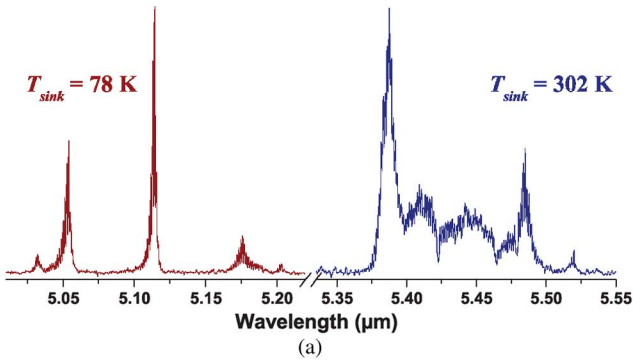


Fig. 6. (a) Representative normalized spectra of the three injector well structure for  $T_{sink} = 78$  K and  $302$  K near threshold. Characteristic temperature  $T_0$  (b) and pulsed wall-plug efficiency (c) for a  $10.4 \mu\text{m} \times 3 \text{ mm}$  ridge laser device.

$173$  K. Wall-plug efficiency—as shown in Fig. 6(c)—peaks at  $20.5\%$  for  $T_{sink} = 80$  K and  $5.1\%$  at  $300$  K.

#### IV. QC LASER WITH TWO INJECTOR WELLS

##### A. Design and Fabrication

To further test such short injector structures, we designed a second laser with only two injector wells and three active region wells. Besides the removal of one injector well, the two laser designs are otherwise similar. The emission energy was

designed to be  $\mathcal{E}_{ph} = 241$  meV ( $\lambda_0 = 5.14 \mu\text{m}$ ) and energy defect designed to be  $\Delta_{inj} = 107$  meV. The total QC period length  $L_p = 274.5 \text{ \AA}$ , for a design field  $E_{field} = 128 \text{ kV/cm}$ . As shown in the Fig. 7 conduction band diagram, the layer sequence is, in angstroms starting from the injection barrier, **35/53/10.5/43/8.5/35/21/28.5/15.5/24.5**, where  $\text{Al}_{0.710}\text{In}_{0.290}\text{As}$  layers are in bold type,  $\text{In}_{0.638}\text{Ga}_{0.362}\text{As}$  layers are in plain type, and layers Si-doped  $n = 1.4 \times 10^{17} \text{ cm}^{-3}$  are underlined; the structure has an active core sheet density  $n_s = 0.96 \times 10^{11} \text{ cm}^{-2}$ . At  $132 \text{ kV/cm}$ , with the upper laser state somewhat isolated from the injector region states, we calculate  $\tau_u = 1.41 \text{ ps}$ ,  $\tau_\ell = 0.23 \text{ ps}$ ,  $\tau_{ul} = 4.55 \text{ ps}$ , and  $z_{ul} = 20.1 \text{ \AA}$ , for a Figure of Merit  $\text{FoM} = 542 \text{ ps \AA}^2$  and  $\text{FoM}^* = 131 \text{ ps \AA}^2 \text{ eV}$ .

The laser was grown by MOVPE with a waveguide structure identical to that described in the previous section. Fabrication and processing were also similar.

##### B. Results and Discussion

Similar to the three well injector design reported in the previous section, LIV data for this design also show NDR, as seen in Fig. 8 for an EL mesa; in this case though, it is much less pronounced. Following the analysis of the previous section, the NDR appears  $3.6 \text{ V}$  ( $26 \text{ kV/cm}$ ) below the designed turn-on voltage. In this design, we calculate that the upper laser state and the second active region state of the upstream active region mix at  $E_{field} = 103 \text{ kV/cm}$ ; here, the difference between the field at which these states align and the designed turn-on field— $25 \text{ kV/cm}$ —is in excellent agreement with the data. However, the states mix to a much less extent, which is consistent with the lower current change associated with the NDR feature.

The two injector well design shows other characteristic features in the LIV data. For example, in Fig. 9 we see two physically separate mechanisms that limit light output. For an applied  $20 \text{ V}$ , we see an increase in differential resistance; the feature is roughly independent of temperature, and it corresponds to a drop in slope efficiency. A second increase in differential resistance is observed, this time at a constant current density of about  $7 \text{ kA/cm}^2$  (independent of temperature). Again, this feature generally corresponds to a decrease in output power. That the first effect appears with constant applied field and the second appears with constant current density is telling of the physical origins. The constant-current feature is the “turn-off” most commonly seen in QC lasers, where a maximum current density is reached based on the intrinsic transit times and the finite amount of doping  $n_s$  of the QC structure [16].

The constant-voltage turn-off feature in Fig. 9 is not as commonly observed. One explanation for this feature arises from examining the injector region configuration relative to the active region at different fields. At  $T_{sink} = 79 \text{ K}$ , the difference between the turn-on voltage of the device and this constant-voltage turn-off is about  $2.1 \text{ V}$  ( $15 \text{ kV/cm}$ ). Our laser was intentionally designed for the lowest state of one active region to be in resonance with the upper laser state of the adjacent downstream active region at threshold, providing efficient transport between active regions and thus decreasing  $\tau_{inj}$ . In this design, these levels are in full resonance when  $E_{field} = 128 \text{ kV/cm}$ .

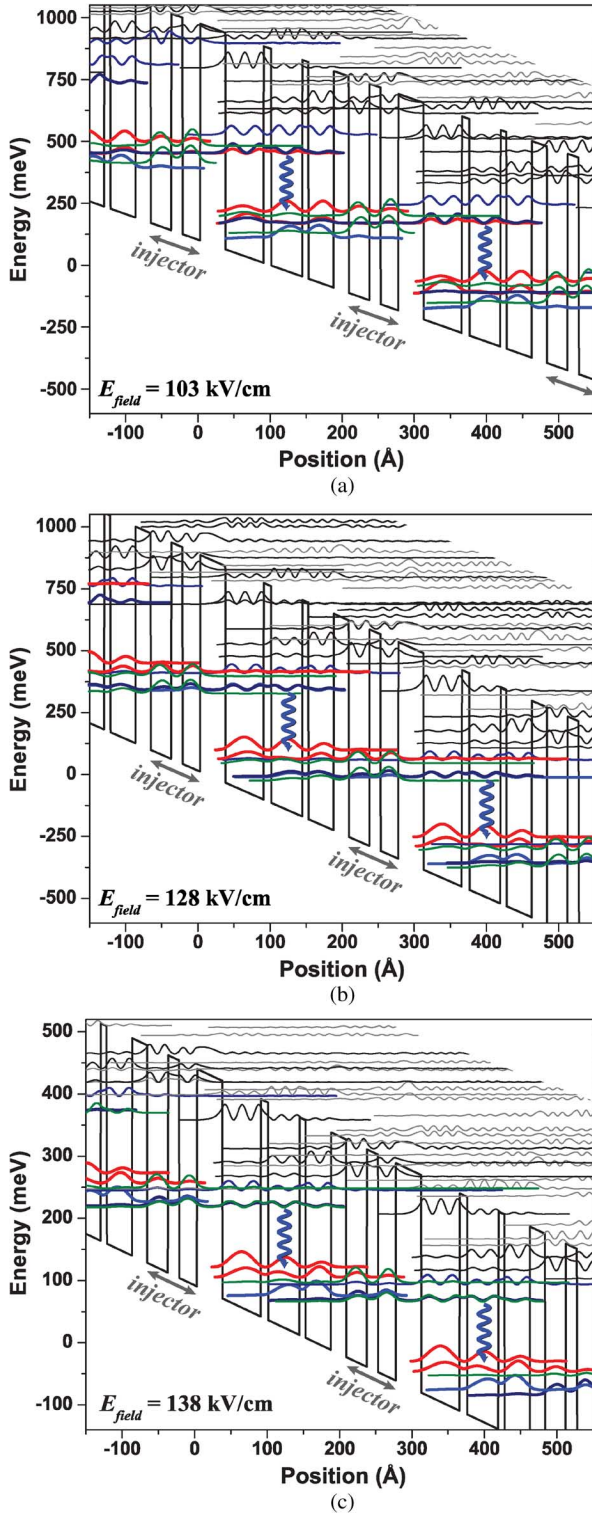


Fig. 7. QC structure with two injector wells and three active region wells. NDR is observed in this structure at  $E_{\text{field}} = 103 \text{ kV/cm}$ , (a). The designed turn-on field is  $128 \text{ kV/cm}$ , (b). Also, an increase in differential resistance is seen in device data consistent with a re-configuration of the band alignment where the upper laser state is in resonance with the injector ground state, as in (c), near  $E_{\text{field}} = 138 \text{ kV/cm}$ .

However, because of the spatial separation of these two states, they remain strongly coupled over only a small field range. At  $E_{\text{field}} = 128 \text{ kV/cm}$ , the lowest injector state is below these

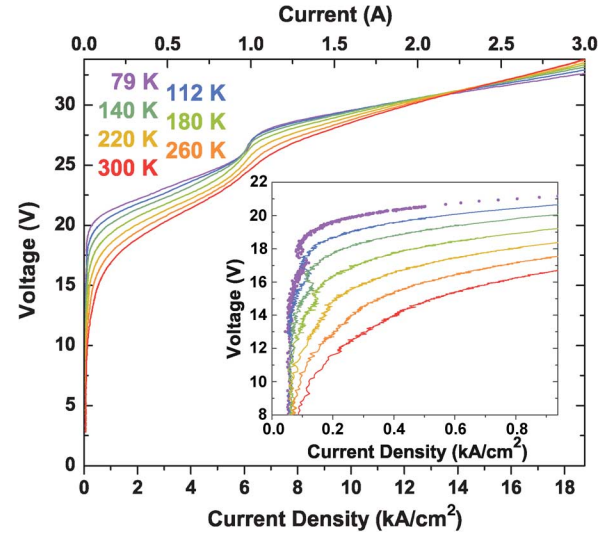


Fig. 8. NDR is also seen in the two injector well design, but it is much less pronounced than in the three injector well design. Here, we see small NDR for a  $0.016 \text{ mm}^2$  EL mesa. The inset is shows the low current region more clearly.

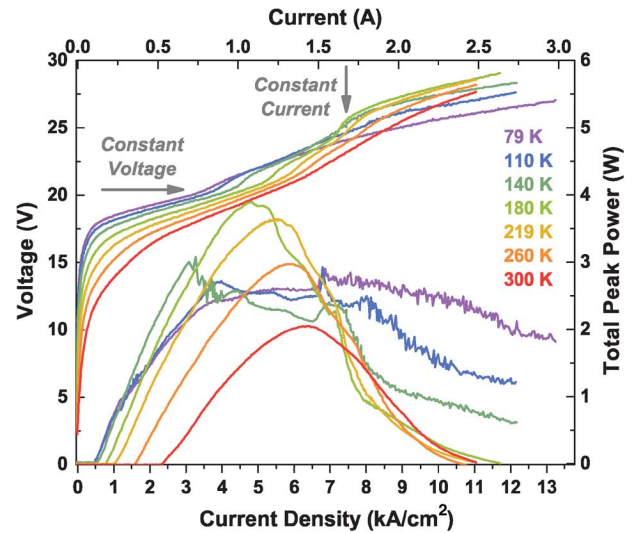


Fig. 9. Pulsed LIV data for a representative two injector well  $7.5 \mu\text{m} \times 3 \text{ mm}$  BH laser device. Two “turn-off” features are seen, one occurring with constant voltage and one with constant current. Pulse instabilities in the light power are also evident at lower temperatures. Because of these instabilities, output power is highest at elevated temperatures. The data shown here are for sampling averaged over  $\sim 15$  pulses.

two aligned states; increasing the field to  $138 \text{ kV/cm}$  puts the lowest injector state and the upper laser state in full resonance. This secondary field alignment and electron path is conceivably slower, as electrons have to travel through an additional state, increasing the differential resistance. The increase in differential resistance observed at constant applied field with variations in temperature may thus arise from these two injector region alignments. The successful operation of both these band alignments is further evidence that electrons can *directly* tunnel from one active region to the next in these short injector structures.

Yet another interesting feature is seen in the Fig. 9 LIV characteristics. Rather than peak output at the lowest temperatures, these lasers have peak output at elevated temperatures (180 K in



this device), while highly unstable pulse behavior at lower temperatures limits average output power. The time evolution of the light pulse over the 100 ns period also indicates highly irregular behavior, with pulse-to-pulse variations on the order of 100 mW at low temperatures. These pulse instabilities are damped with increasing temperature, and they disappear around 140 K.

In QC structures, electric field profiles are largely assumed to be homogenous when the doping density is low, or periodic but stable when the doping density is higher. However, charge instabilities have long been known to exist in superlattice structures [18]. Intuitively, charge instabilities can result when local disruptions of the charge density locally perturb the field, leading to electric field domains. The highly nonlinear event of lasing onset is expected to exacerbate this instability, and in these minimalized QC structures, these instabilities are now more apparent.

Both of the previous features—constant-voltage turn-off and pulse instabilities—result from the highly discrete nature of the individual quantum states in our structure. In actuality, we have composed a QC structure out of only six relevant states: a ground state for each of the five quantum wells in the QC period and one quantum well first-excited state that is the upper laser state. Having only six states spread across  $\Delta_{\text{inj}} = 107$  meV is unusual for QC structures; a comparable conventional design with a four well active region and seven injector wells would have 12 states spread across the same  $\Delta_{\text{inj}}$ . In this situation, we see the effect of the highly discrete injector region states; the positioning of individual states matters more than ever.

### C. Device Performance

Even with all of the unique features of the present device, performance is comparable to the best designs reported in the literature. We observe lasing at  $\lambda_0 \approx 5.0 \mu\text{m}$  for  $T_{\text{sink}} = 79$  K and at  $\lambda_0 \approx 5.2 \mu\text{m}$  at room temperature, as shown in Fig. 10(a). For the BH laser device described by the Figs. 9 and 10 data, pulsed total output power peaks at 3.9 W at 180 K, while room temperature output power is 1.4 W. Low temperature output power in these devices is severely limited by the pulse instabilities previously discussed. Threshold current density is as low as  $460 \text{ A/cm}^2$  at 80 K, and grows to  $2.3 \text{ kA/cm}^2$  at room temperature. Fig. 10(b) shows threshold behavior similar to the three injector well design. As in the three injector well device, the  $T_0$  approaching room temperature is relatively low at 113 K; the low temperature  $T_0 = 305$  K. Wall-plug efficiency—as shown in Fig. 10(c)—peaks at 23.0% for  $T_{\text{sink}} = 140$  K and 7.6% at 300 K. Again, wall-plug efficiency at low temperatures is limited by pulse instabilities.

## V. CONCLUSION

We have presented our study on short injector region QC lasers, taking the approach of shrinking the conventional (approximately) seven quantum well injector region to only two or three wells. Making the active core gain region “denser” with optical transitions by shortening the QC period length in principle leads to improvement in performance metrics associated with output power and efficiency. Through this study of short injectors, we have observed several unique effects in QC lasers.

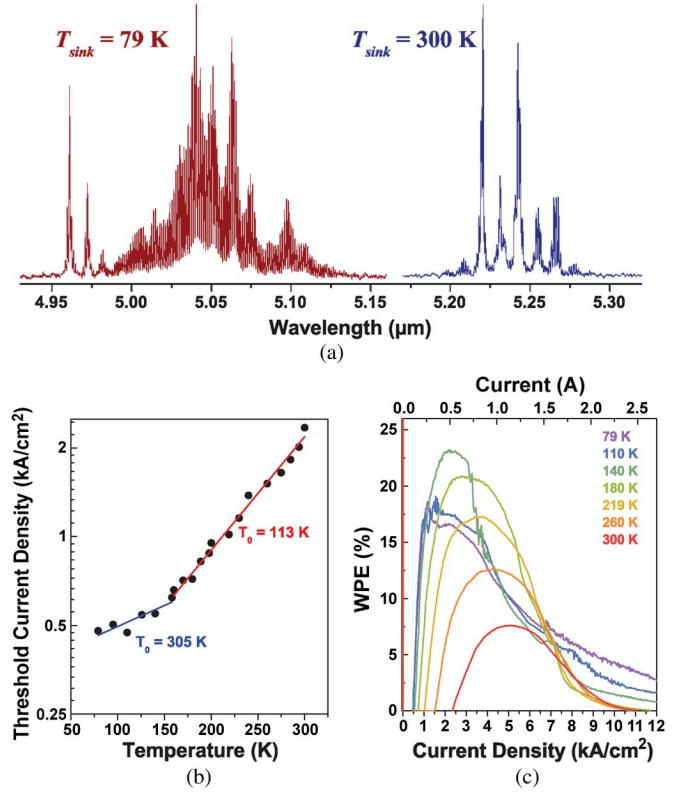


Fig. 10. (a) Representative normalized spectra of the two injector well structure for  $T_{\text{sink}} = 79$  K and 300 K near threshold. Characteristic temperature  $T_0$  (b) and pulsed wall-plug efficiency (c) for a two injector well  $7.5 \mu\text{m} \times 3 \text{ mm}$  BH laser device.

While the understanding of these effects augment our knowledge of QC laser processes in general, they are particularly relevant with regard to developing high performing lasers based on the short injector concept.

Pronounced NDR is observed in spontaneous emission EL devices; furthermore, the presence of stimulated emission in laser devices of the same QC design impacts the operating configuration of the laser band structure. Turn-off mechanisms—increases in differential resistance—are observed at constant voltages with temperature, in addition to the more conventional turn-off features observed at constant current. These effects can be attributed to two distinctive characteristics of the short injector designs presented here: enhanced “coupling” of neighboring active regions due to the close proximity afforded by the extremely abbreviated injector regions; and the highly discrete nature of the injector region energy states.

The observation of these new phenomena provides additional insight into the mechanisms of QC laser operation. The pronounced NDR of the three injector well laser and its successful operation at a lowered field demonstrates the dynamic effect of stimulated emission on electron distributions and energy state lifetimes. Indeed, much of what we have observed confirms that such abbreviated QC structures behave in many ways similar to the classical semiconductor superlattice. For example, the highly discrete nature of individual states becomes particularly relevant, as well as the need to damp pulse instabilities [19] associated with shifting charge distributions.



Clearly challenges remain with optimizing QC laser injector regions. In addition to the need to damp pulse instabilities, we have observed relatively low  $T_0$  values in short injector structures (see also [20]) that are beginning to appear to be systematic. Understanding the origin of this diminished performance at elevated temperatures will help to realize the full potential of short injector QC structures.

## REFERENCES

- [1] A. Lyakh, C. Pflügl, L. Diehl, Q. J. Wang, F. Capasso, X. J. Wang, J. Y. Fan, T. Tanbun-Ek, R. Maulini, A. Tsekoun, R. Go, and C. K. N. Patel, "1.6 W high wall plug efficiency, continuous-wave room temperature quantum cascade laser emitting at 4.6  $\mu\text{m}$ ," *Appl. Phys. Lett.*, vol. 92, p. 111110, 2008.
- [2] M. Razeghi, "High-power high-wall plug efficiency mid-infrared quantum cascade lasers based on InP/GaInAs/InAlAs material system," *Proc. SPIE*, vol. 7230, p. 723011, 2009.
- [3] D. Hofstetter, M. Beck, T. Aellen, and J. Faist, "High-temperature operation of distributed feedback quantum-cascade lasers at 5.3  $\mu\text{m}$ ," *Appl. Phys. Lett.*, vol. 78, no. 4, pp. 396–398, 2001.
- [4] M. Beck, D. Hofstetter, T. Aellen, J. Faist, U. Oesterle, M. Illegems, E. Gini, and H. Melchior, "Continuous wave operation of a mid-infrared semiconductor laser at room temperature," *Science*, vol. 295, no. 5553, pp. 301–305, 2002.
- [5] S. S. Howard, Z. Liu, and C. F. Gmachl, "Thermal and stark-effect roll-over of quantum-cascade lasers," *IEEE J. Quantum Electron.*, vol. 44, no. 3–4, pp. 319–323, Mar.–Apr. 2008.
- [6] M. C. Wanke, F. Capasso, C. Gmachl, A. Tredicucci, D. L. Sivco, A. L. Hutchinson, S.-N. G. Chu, and A. Y. Cho, "Injectorless quantum-cascade lasers," *Appl. Phys. Lett.*, vol. 78, pp. 3950–3952, 2001.
- [7] A. Friedrich, G. Boehm, and M. C. Amann, "Short-wavelength intersubband staircase lasers, with and without AlAs-blocking barriers," *Semicond. Sci. Technol.*, vol. 22, pp. 218–221, 2007.
- [8] S. Katz, A. Friedrich, G. Boehm, and M.-C. Amann, "Continuous wave operation of injectorless quantum cascade lasers at low temperatures," *Appl. Phys. Lett.*, vol. 92, p. 181103, 2008.
- [9] H. Luo, S. R. Laframboise, Z. R. Wasilewski, G. C. Aers, H. C. Liu, and J. C. Cao, "Terahertz quantum-cascade lasers based on a three-well active module," *Appl. Phys. Lett.*, vol. 90, no. 4, p. 041112, 2007.
- [10] M. A. Belkin, J. A. Fan, S. Hormoz, F. Capasso, S. P. Khanna, M. Lachab, A. G. Davies, R. C. Iotti, and E. H. Linfield, "Terahertz quantum cascade lasers with copper metal-metal waveguides operating up to 178 K," *Opt. Expr.*, vol. 16, no. 5, pp. 3242–3248, 2008.
- [11] R. Köhler, A. Tredicucci, F. Beltram, H. E. Beere, E. H. Linfield, A. G. Davies, D. A. Ritchie, R. C. Iotti, and F. Rossi, "Terahertz semiconductor-heterostructure laser," *Nature*, vol. 417, no. 6885, pp. 156–159, May 9, 2002.
- [12] K. J. Franz, "New quantum cascade laser architectures: II-VI quantum cascade emitters, high-space lasing, and short injectors" Ph.D. dissertation, Princeton Univ., Princeton, NJ, Jun. 2009 [Online]. Available: <http://www.kjfranz.us/thesis>
- [13] J. Faist, "Wallplug efficiency of quantum cascade lasers: Critical parameters and fundamental limits," *Appl. Phys. Lett.*, vol. 90, p. 253512, 2007.
- [14] T. Gresch, M. Giovannini, N. Hoyer, and J. Faist, Quantum Cascade Lasers With Large Optical Waveguides vol. 18, no. 3, pp. 544–546, 2006.
- [15] C. Sirtori, F. Capasso, J. Faist, A. Hutchinson, D. Sivco, and A. Cho, "Resonant tunneling in quantum cascade lasers," *IEEE J. Quantum Electron.*, vol. 34, no. 9, pp. 1722–1729, Sep. 1998.
- [16] T. Aellen, M. Beck, N. Hoyler, M. Giovannini, J. Faist, and E. Gini, "Doping in quantum cascade lasers. I. InAlAs-InGaAs/InP midinfrared devices," *J. Appl. Phys.*, vol. 100, no. 4, p. 043101, 2006.
- [17] K. J. Franz, D. Wasserman, A. J. Hoffman, D. C. Jangraw, K.-T. Shiu, S. R. Forrest, and C. Gmachl, "Evidence of cascaded emission in a dual-wavelength quantum cascade laser," *Appl. Phys. Lett.*, vol. 90, no. 9, p. 091104, 2007.
- [18] K. Leo, *High-Field Transport in Semiconductor Superlattices*. Berlin: Springer, 2006.
- [19] P. G. Savvidis, B. Kolasa, G. Lee, and S. J. Allen, "Resonant crossover of Terahertz loss to the gain of a Bloch oscillating InAs/AlSb superlattice," *Phys. Rev. Lett.*, vol. 92, no. 19, p. 196802, May 2004.
- [20] M. D. Escarra, A. J. Hoffman, K. J. Franz, S. S. Howard, R. Cendejas, X. Wang, J.-Y. Fan, and C. Gmachl, "Quantum cascade lasers with voltage defect of less than one longitudinal optical phonon energy," *Appl. Phys. Lett.*, vol. 94, no. 25, p. 251114, 2009.



**Kale J. Franz** (S'02) received the B.S. degree in engineering physics with Highest Scholastic Honors from the Colorado School of Mines, Golden, CO, in 2004, and the Ph.D. degree in electrical engineering from Princeton University, Princeton, NJ, in 2009, under the supervision of Prof. C. Gmachl. At Princeton, his research focused on improving the capabilities and performance of quantum cascade laser technology.

From 2001 to 2002, he was an intern with the U.S. Department of Energy Office of Science, working on science and education policy initiatives. From 2003 to 2004, he conducted research on the growth and fabrication of carbon nanotubes, for the primary application of hydrogen storage. He has authored or coauthored more than 20 publications and conference proceedings along with 40 presentations, and holds three patents and provisional applications.

While at Princeton University, his work was supported by a National Science Foundation Graduate Research Fellowship and the Princeton University Wallace Fellowship.



**Peter Q. Liu** received the B.E. degree in electronic engineering and graduated with highest honors from Tsinghua University, Beijing, China, in 2007. He is currently a Ph.D. degree student with the Department of Electrical Engineering, Princeton University, Princeton, NJ.

His ongoing research under the supervision of Prof. C. Gmachl focuses on improving the performance of quantum cascade lasers. His undergraduate thesis focused on the electronic characteristics of graphene.

At Princeton, his work has been supported by a Francis Robbins Upton Fellowship.



**James J. J. Raftery** received the B.S.E. degree in electrical engineering (*cum laude*) from Princeton University, Princeton, NJ, in 2006, and the M.S. degree in electrical engineering from the California Institute of Technology (Caltech), Pasadena, in 2008.

As an undergraduate at Princeton University, he worked under the guidance of Prof. C. Gmachl on waveguide design for quantum cascade lasers. As a graduate student at Caltech, he worked under the guidance of Prof. A. Yariv on broad-area photonic crystal lasers and coupled resonator optical waveguides. He currently works in the Intellectual Property Group at the law firm Jones Day.



**Matthew D. Escarra** (S'05) received the B.S. degree in electrical engineering from Rice University, Houston, TX, in 2006, graduating with honors. He is presently a Ph.D. degree candidate with the Department of Electrical Engineering, Princeton University, Princeton, NJ. As an undergraduate at Rice University, he was involved in the development of a new generation of photoconductive terahertz antennas for coupling to metal wire waveguides. As a graduate student at Princeton University, he has worked under the guidance of Prof. C. Gmachl.

His research focuses on high-efficiency and high-performance quantum cascade lasers for sensing applications.



**Anthony J. Hoffman** (S'05) received the B.S. degree with honors in physics from the University of Maryland, Baltimore County, in 2004. He received the Ph.D. degree in electrical engineering from Princeton University, Princeton, NJ, in 2009. His thesis work was on high-performance quantum cascade lasers and midinfrared metamaterials.

He is currently a Postdoctoral Research Associate at Princeton University working on circuit quantum electrodynamics.



**Scott Sheridan Howard** (S'05–M'09) received the Ph.D. degree from the Department of Electrical Engineering, Princeton University, Princeton, NJ, in 2008. His research at Princeton University focused on high-performance quantum cascade laser design, fabrication, and characterization.

He is currently a Postdoctoral Research Associate with the School of Applied and Engineering Physics, Cornell University, Ithaca, NY, where his research focuses on fiber-based nonlinear medical imaging.

Dr. Howard is the 2007 Newport Award winner for excellence in photonics research at Princeton University.



**Yu Yao** received the B.S. and M.S. degrees in electrical engineering from Tsinghua University, Beijing, China, in 2004 and 2006, respectively. She is currently working toward the Ph.D. degree with the Department of Electrical Engineering, Princeton University, NJ.

Her research focuses on high-performance quantum cascade lasers.



**Yamac Dikmelik** (S'93–M'05) received the B.S. and M.S. degrees in electrical engineering from Bilkent University, Ankara, Turkey, in 1996 and 1998, respectively, and the Ph.D. degree in electrical engineering from Johns Hopkins University, Baltimore, MD, in 2004.

He was a Postdoctoral Fellow with the Department of Materials Science and Engineering, Johns Hopkins University, from 2004 to 2007. He is presently an Assistant Research Scientist with the Department of Electrical and Computer Engineering, Johns Hop-

kins University.



**Xiaojun Wang** received the Ph.D. degree in physics from XiaMen University, China, in 1994. As part of his Ph.D. dissertation and his postdoctoral research, he worked on the high-power 980-nm and 808-nm lasers at the Institute of Semiconductors, Chinese Academy of Sciences, from 1992 to 1997.

In February 1998, he joined the Electrical Engineering Department, University of Maryland, Baltimore County, as a Research Associate and then Research Scientist, working on InP-based optoelectronic components for optical fiber communication.

In November 2000, he joined Nortel Networks in Massachusetts as a Senior Device Engineer, working on the 1310-nm single-transverse mode pump laser and MEMS-based C/L band, widely tunable high-power external cavity laser. In January 2003, he joined AdTech Optics, Inc., City of Industry, CA. He currently serves as Director of Chip Development, focusing on commercialization of the midinfrared quantum cascade lasers. He has authored or coauthored more than 70 referred publications.

**Jen-Yu Fan** received the Ph.D. degree in electrical engineering from the University of Maryland, Baltimore County, in 1999. His dissertation concentrated on the demonstration of all-optical 3R devices. As part of his research project, he implemented InP-based components for high-speed photonic switching in a photonic IP/ATM system, demultiplexing/multiplexing for TDM systems, wavelength converters for WDM systems, and DWDM broadband switching and optical interconnection for optical communications. He designed and fabricated the state-of-the-art building blocks (SOAs, DFBs/DBRs, Mach–Zehnder) to be implemented into edge/surface emitting lasers, mode converters, wavelength converters, optical logic gates, active filters, and optical delay lines.

Following his Ph.D. degree work, he joined Nanovation Technologies, Inc., Evanston, IL, as a Member of Research Staff, investigating a new generation of optical modulators. From 2000 to 2002, he was with LightCross, Inc., Monterey Park, CA, where he managed and worked on the development program for the design of high-performance photonic-integrated circuits based on AWG, VOA, power splitter, and waveguide components on silicon-on-insulator (SOI) material. Since 2002, he has been with AdTech Optics, Inc., City of Industry, CA, where he works on InP-based lasers and modules. His projects have included the fabrication of embedded grating structures for high-performance lasers such as DFBs, electroabsorption modulated lasers (EML), FM lasers, and FM laser-based modulation for microwave–photonic links. Presently, his main objectives include manufacturing of FP/DFB/DBR quantum cascade lasers (QCLs) in the mid-IR to far-IR spectral range with high output powers. He has authored or coauthored more than 50 refereed publications and 70 conference publications and holds one U.S. patent.



**Jacob B. Khurgin** received the M.S. degree in optics from the Institute of Fine Mechanics and Optics, St. Petersburg, Russia, in 1979. He received the Ph.D. degree in electrophysics from the Polytechnic Institute of New York in January 1987.

In 1980, he immigrated to the U.S. and joined Philips Laboratories of NV Philips, Briarcliff Manor, NY. For eight years, he worked on miniature solid-state lasers, II–VI semiconductor lasers, various display and lighting fixtures, X-ray imaging, and small appliances. In January 1988, he joined the Electrical Engineering Department, Johns Hopkins University, Baltimore, MD, where he is currently a Professor. His research topics over the years have included an eclectic mixture of optics of semiconductor nanostructures, nonlinear optical devices, optical communications, microwave photonics, and condensed matter physics. Currently, he is working in the areas of midinfrared lasers, plasmonics, laser cooling, phonon engineering for high-frequency transistors, coherent optical communications, and slow light propagation. His publications include five book chapters, one book edited, more than 200 papers in refereed journals, and 14 patents.

Prof. Khurgin is a Fellow of the Optical Society of America.



**Claire Gmachl** (S'94–A'95–SM'00) received the Ph.D. degree (*sub auspiciis praesidentis*) in electrical engineering from the Technical University of Vienna, Austria, in 1995.

In 1996, she joined Bell Laboratories, Lucent Technologies, Murray Hill, NJ, as a Postdoctoral Member of Technical to work on quantum cascade laser devices and microcavity lasers. In March 1998, she became a Member of Technical Staff in the Semiconductor Physics Research Department and a Distinguished Member of Staff in 2002.

In September 2003, she joined Princeton University, Princeton, NJ, as an Associate Professor with the Department of Electrical Engineering and adjunct faculty to PRISM. In 2007, she became a full Professor. She is the Director of MIRTHE, the NSF Engineering Research Center on Mid-InfraRed Technologies for Health and the Environment formed in 2006. She has authored or coauthored more than 170 publications, has given more than 100 presentations at conferences and seminars, and holds 26 patents.

Dr. Gmachl is an Associate Editor for *Optics Express* and a member of the IEEE/LEOS Board of Governors. She is a 2005 MacArthur Fellow and a corresponding member abroad of the Austrian Academy of Sciences.